

Particle Image Velocimetry Measurements of Turbulent Flow Within Outdoor and Indoor Urban Scale Models and Flushing Motions in Urban Canopy Layers

Hiroshi Takimoto · Ayumu Sato · Janet F. Barlow ·
Ryo Moriwaki · Atsushi Inagaki · Shiho Onomura ·
Manabu Kanda

Received: 20 May 2010 / Accepted: 24 March 2011 / Published online: 21 April 2011
© Springer Science+Business Media B.V. 2011

Abstract We investigate the spatial characteristics of urban-like canopy flow by applying particle image velocimetry (PIV) to atmospheric turbulence. The study site was a Comprehensive Outdoor Scale MOdel (COSMO) experiment for urban climate in Japan. The PIV system captured the two-dimensional flow field within the canopy layer continuously for an hour with a sampling frequency of 30 Hz, thereby providing reliable outdoor turbulence statistics. PIV measurements in a wind-tunnel facility using similar roughness geometry, but with a lower sampling frequency of 4 Hz, were also done for comparison. The turbulent momentum flux from COSMO, and the wind tunnel showed similar values and distributions when scaled using friction velocity. Some different characteristics between outdoor and indoor flow fields were mainly caused by the larger fluctuations in wind direction for the atmospheric turbulence. The focus of the analysis is on a variety of instantaneous turbulent flow structures. One remarkable flow structure is termed ‘flushing’, that is, a large-scale upward motion prevailing across the whole vertical cross-section of a building gap. This is observed intermittently, whereby tracer particles are flushed vertically out from the canopy layer. Flushing phenomena are also observed in the wind tunnel where there is neither thermal stratification nor outer-layer turbulence. It is suggested that flushing phenomena are correlated with the passing of large-scale low-momentum regions above the canopy.

H. Takimoto (✉) · A. Inagaki · S. Onomura · M. Kanda
Department of International Development Engineering, Tokyo Institute of Technology, Tokyo, Japan
e-mail: takimoto.h.aa@m.titech.ac.jp

A. Sato
Environmental Science Research Laboratory, Central Research Institute of Electric Power Industry,
Chiba, Japan

J. F. Barlow
Department of Meteorology, University of Reading, Reading, UK

R. Moriwaki
Department of Civil and Environmental Engineering, Ehime University, Ehime, Japan

Keywords Flushing · Organized structure · Outdoor scale model · Particle image velocimetry · Urban canopy layer

1 Introduction

Investigation of the flow fields inside urban canopy layers is very important for the understanding of heat exchange and scalar dispersion in cities. They have been extensively studied in the last decade or so, mostly using single-point sensors such as ultrasonic anemometers. Single-point sensors can provide accurate and long-term datasets that are effective for the development of canopy-flow models. However, the flow statistics in urban canopy layers vary strongly with location. For a clearer understanding of complex canopy flow, it is desirable to implement spatial measurements. Although there are a few pioneering examples of spatial measurements of canopy flows using multiple sensors aligned in two-dimensional arrays (e.g. Rotach 1995; Louka et al. 2002; Eliasson et al. 2006; Sugawara et al. 2006; Klein and Clark 2007), the number of measurement points is still restricted to between 10 and 20 at most.

In this study, the spatial characteristics of urban-like canopy flow with high Reynolds number were investigated using field measurements from particle image velocimetry (PIV). PIV measures fluid velocity in two-dimensional cross-sections with very high spatial resolution, and this technique has been utilized in many applications of turbulence measurements (e.g. Adrian et al. 2000; Liu et al. 2003; Reynolds and Castro 2008). However, most PIV measurements are conducted in laboratories, and application to atmospheric turbulence is rare (e.g. Zhu et al. 2006). This is due to the difficulties in performing flow visualization in the atmospheric environment, caused by highly fluctuating wind direction and wind speed. The first step in our study was to develop a PIV system for the measurement of atmospheric turbulence within and above an outdoor urban scale model (COSMO). Not only the difficulties arising from the large fluctuations in wind speed and direction, but also the extensive scale of our measuring section, make it difficult to achieve homogeneous seeding of tracer particles. Observations were made using this system, and the spatial distributions of turbulence statistics, and the characteristics of instantaneous flow structures were investigated. Flow structures inside canopy layers are often identified as unsteady motions, and are different from mean flow structures (e.g. Louka et al. 2000; Eliasson et al. 2006). The dispersion of scalars is also an unsteady process, so the understanding of the temporal change of flow fields is important. Various types of instantaneous flow structures and their complexity were confirmed in our study, and our attention is especially focussed on large-scale upward motions, a kind of ‘flushing’ phenomenon in canopy layers.

Recent large-eddy simulation studies (e.g. Kanda et al. 2004; Kanda 2006) revealed the existence of a longitudinally elongated turbulence structure in urban boundary layers. The importance of such a structure to momentum exchange has also been confirmed experimentally (Inagaki and Kanda 2010). This turbulent organized structure (TOS) is not visible in mean flow fields, and the relationship between canopy flow and TOS remains unclear because of the lack of knowledge of instantaneous flow fields. We here discuss the connections between flushing motions in canopy layers and the TOS above them. It is noted that, outdoor PIV measurements are only possible at night, and so results from our study do not include buoyant effects because of solar radiation.

Wind-tunnel experiments were performed using the same roughness element geometry as the field experiment to compare with results for the COSMO model. The wind-tunnel experiments were conducted using a second PIV system (Dantec Dynamics), which is a typical system for laboratory experiments.

2 Experimental Methods

2.1 Field Experiment

The field PIV experiments were implemented at an outdoor urban scale model (COSMO, Fig. 1a), which was constructed as a simplified model city to exclude the influences of human activity and heterogeneity of the surface geometry. The study site is located on the campus of Nippon Institute of Technology, Japan ($39^{\circ}04'N$, $139^{\circ}07'E$). The building models are 1.5 m concrete cubes, and 32×16 blocks are regularly aligned in a square array on a $100m \times 50m$ flat concrete plate. Both the plan area index and the frontal area index are 0.25, and the aspect ratio of canopy height (H) to street width (W) is 1.0. The longitudinal axis (north–west to south–east axis) of the site is designed to correspond with the prevailing wind direction of the Asian monsoon during summer and winter. Hereinafter, the longitudinal axis, the lateral axis and the vertical axis of the site are described as the x , y and z axes, respectively, where u , v and w are the velocity components in the x , y and z directions, respectively. The experiments in COSMO have provided supplementary information to laboratory and field experiments under realistic conditions of sunshine and wind fluctuations [e.g. Kawai et al. (2007) for the heat budget, Kanda et al. (2007) and Kanda and Moriizumi (2009) for the urban land surface parameterization, Inagaki and Kanda (2008) for the turbulent flow similarity, Inagaki and Kanda (2010) for the turbulent structure, and Nakayoshi et al. (2009) for the rainfall interception]. This scale model is an essential part of our study, since PIV experiments in real cities are difficult to realize as they involve the use of a high-power laser and a massive amount of tracer particles. Further information about COSMO is provided in the above references.

A PIV measurement was carried out at the COSMO site on 4 September 2008, from 2106 JST (Japan Standard Time) to 2206 JST; sunset was at 1807 JST, and there were no clear trends in wind direction or wind speed during the measurement. The measurement period

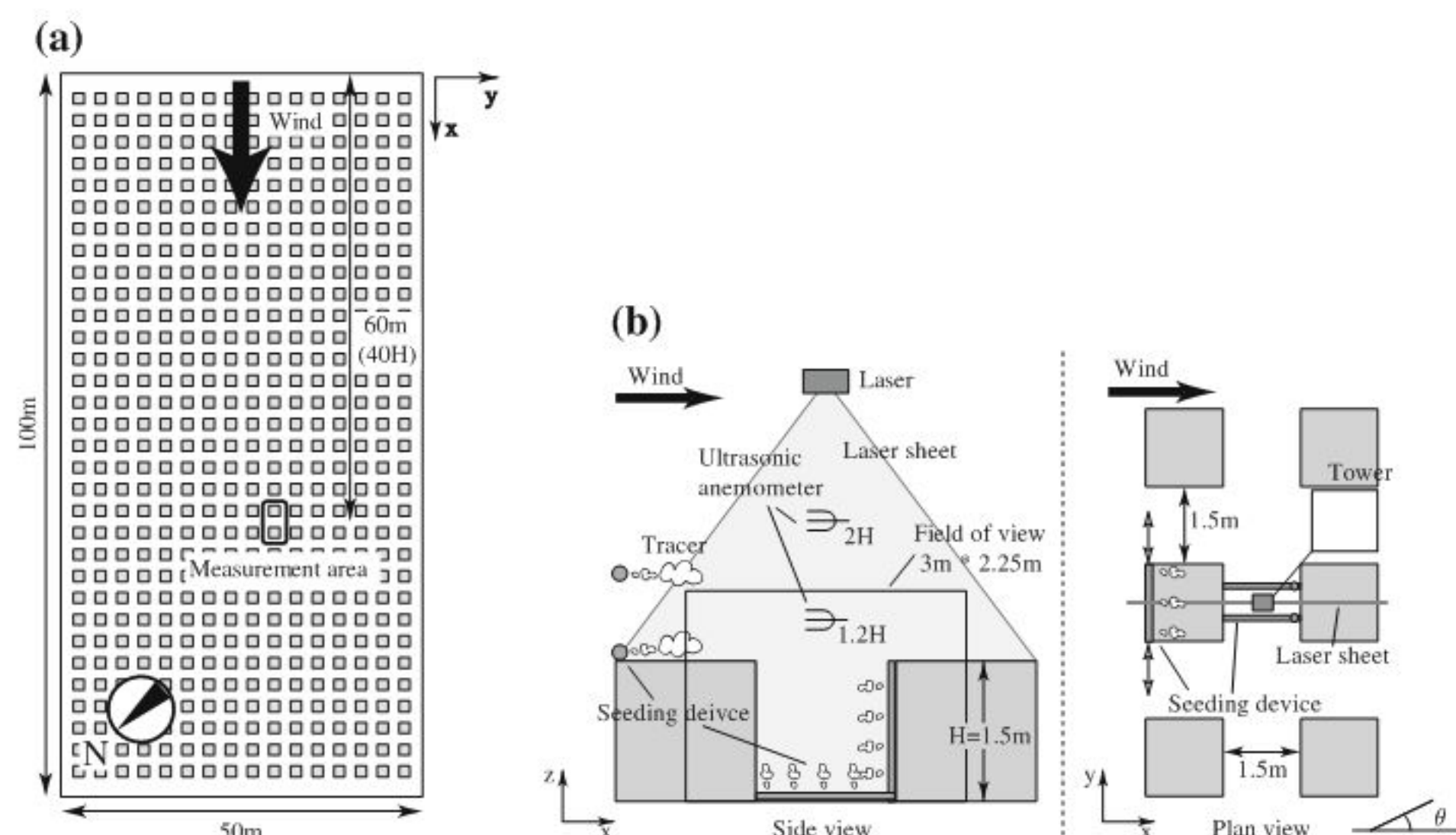


Fig. 1 Schematic view of the COSMO site. **a** Plan view of COSMO. Wind direction is usually south-easterly in summer season. **b** Set-up of the outdoor experiment. Ultrasonic anemometers were installed at heights of $1.2H$ and $2H$ at the centre point of the building gap

was set to 60 min to ensure reliable statistics given the atmospheric conditions (Stull 1988). The measurement section was a vertical cross-section of 3-m length and 2.25-m height at the centre of a building gap (Fig. 1), and it is located 60 m ($40H$) downstream from the edge of the COSMO site. The estimated depth of the internal boundary layer is $3H$ – $4H$ according to the observations of Inagaki and Kanda (2008) at this site. For flow visualization, a continuous-wave Nd:YAG laser (1 W) was mounted on a tower at a height of 5 m; the diameter of the scaffolding poles used for the tower was 50 mm and the tower was placed at the downstream side of the measurement section. The tracer particles used in the experiment were glycol droplets, and were supplied from multiple fog generators (Antari, V1 fogger) through perforated PVC pipes (diameter $\phi = 20$ mm) that were set at the upstream side of the measurement section. These seeding pipes were built up as movable line sources to cope with the highly fluctuating wind direction, and were placed perpendicular to the x -axis of the site. Another seeding pipe was also installed inside the canopy layer. The outlet velocity of the smoke was manually adjusted to around 0.3 m s^{-1} . The diameter of each hole in the seeding pipes was only 3 mm, and the disturbances to the flow field can be neglected. A schematic view of the PIV set-up is shown in Fig. 1. The resolution of the CCD camera (Hitachi Kokusai Electric, KP-F120CL) was 1392×1040 pixels, and the frame rate was 30 Hz, a resolution that corresponds to 2.1 mm per pixel in actual scale. Therefore, it was not possible to capture each tracer particle, and the tracer concentrations are tracked, instead. In a typical PIV analysis, particle images are divided into small windows, and the distributions of tracer particles in each window are traced by calculating the cross-correlation function for sequential images. However, the method using the cross-correlation function tends to place priority on the displacements of higher brightness pixels than dark pixels, since it computes the accumulation of the product of each brightness value. Although this algorithm is suitable for tracking finely resolved particles, it is not the best way to track the contrasting patterns of tracer particles. Thus, the grey-level difference accumulation method, which computes the summation of the absolute value of the grey-level difference between two images (Kaga et al. 1992), was adopted for estimating the correlation peak. The small window used in the image analysis is called the interrogation window, and a vector obtained by PIV measurement is the spatially-averaged value within this window. The interrogation window size in the COSMO experiment was set to $88.9 \times 88.9 \text{ mm}^2$ considering the balance between measurement accuracy and spatial resolution.

Two ultrasonic anemometers (Kaijo) were utilized to measure three-dimensional wind speed. The span of the probes is 50 mm, and they were set at heights of $1.2H$ and $2H$ at the centre point of the building gap. Sampling frequency of the sonics was 50 Hz. At $z = 2H$, the mean wind speed during the measurement was $\bar{u}_{2H} = 0.73 \text{ m s}^{-1}$, and the mean wind direction $\bar{\theta}$ was 26.2° . Here, θ represents the wind direction, which is zero when the airflow is parallel to the x -axis. The magnitude of the scalar velocity was $\sqrt{u^2 + v^2} = 0.83 \text{ m s}^{-1}$. For regular arrays of cubes, the level $z = 2H$ is expected to be in the inertial sublayer (e.g. Cheng and Castro 2002; Inagaki and Kanda 2008). The roughness Reynolds number $Re_* (= u_* z_0 / v)$ was 810. The value of the aerodynamic roughness length $z_0 = 0.1 \text{ m}$ was derived by Inagaki and Kanda (2008), and the friction velocity u_* was calculated from the sonic data at $z = 2H$ as $u_* = \sqrt{-\bar{u}' w'}$. This estimate of friction velocity is taken from Inagaki and Kanda (2008), who showed the effectiveness of the scaling using $\sqrt{u' w'_{2H}}$. Although the assumption of constant flux with height in the inertial sublayer is not always true, it is appropriate to use the same definition of friction velocity for both the COSMO and the wind-tunnel models for a fair comparison. If the spanwise velocity v is taken into account for the calculation of u_* , then Re_* becomes 1.09 times larger than this value. Atmospheric stability during the

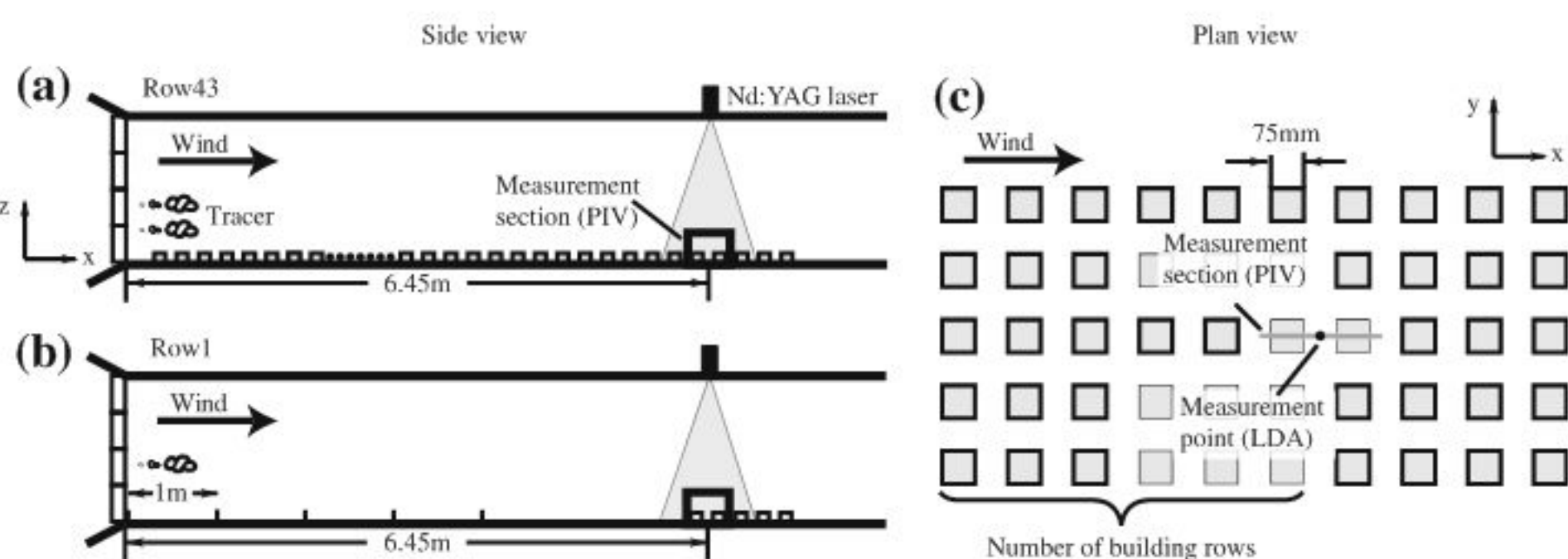


Fig. 2 Schematic view of the wind-tunnel experiments. **a** Set-up of the wind tunnel for the case of the longest building array (Row43 case). **b** Same as (a), but for the shortest building array (Row1 case). **c** Plan view of the measurement section. Number of building rows was counted from the upstream side of the measurement section

measurement was moderately unstable, with $z'/L = -0.146$, where L is the Obukhov length, $z' (= z - d)$ is the effective height, while the displacement height $d = 0.46H$ was calculated from Macdonald et al. (1998).

2.2 Wind-Tunnel Experiments

Experiments in a wind tunnel were held at the Central Research Institute of Electric Power Industry, Japan. The test section of the wind tunnel was 10 m long with a cross-sectional area of 1 m × 1 m. Styrofoam cubes ($H = 75$ mm) were used as building models, and they were aligned in the same way as COSMO. The building array consisted of 47 rows in the streamwise direction, and five rows in the spanwise direction (Fig. 2). The PIV measurement section was a vertical cross-section 288 mm × 219 mm at the centre of a building gap, located 6.45 m ($85H$) downstream from the entrance of the wind tunnel, i.e. between the 43rd and 44th building rows (Row43 case). The last three rows were placed so as to prevent sudden changes of boundary conditions behind the measurement section. In the measurement section, we adopt the coordinates where $x = 0$ lies at the leeward wall of the upstream block, $y = 0$ at the lateral centre of the building gap and $z = 0$ at floor level. Mean wind speed at a height of $2H$ was 0.96 m s^{-1} , and thermal stratification was set to neutral by maintaining both air and floor temperatures at 20°C .

Tracer particles were released from the entrance of the wind tunnel through a perforated PVC pipe, and were illuminated by a pulsed Nd:YAG laser (120 mJ per pulse, New Wave Research). Double-pulsed images were taken for 3 min by a CCD camera (Hitachi Kokusai Electric, KP-F120CL, 1344×1024 pixel) at a rate of 4 Hz. Hence, a total of 720 velocity vector maps was obtained. The interval of the double pulse was set to 2.5 ms, and the interrogation window size was 32 pixel × 32 pixel, equal to $6.9 \times 6.9 \text{ mm}^2$.

The vertical profiles of u and w were measured using a two-dimensional laser Doppler anemometer (LDA; Dantec Dynamics) at the centre of the building gap. The diameter of the LDA probe is 14 mm. Measurement time was 90 s for each point. From the profiles of streamwise velocity, boundary-layer depth, where the flow velocity is 99% of the free-stream, was estimated to be around $4H$. The roughness Reynolds number Re_* was 64, where z_0 and u_* were obtained by applying the logarithmic law to the profile of u . This value of Re_* is much larger than the range of critical roughness Reynolds number 1–5.4 proposed by Snyder and Castro (2002) and Uehara et al. (2003), above which Reynolds number

Table 1 Experimental conditions for COSMO and the wind-tunnel (Row43 case)

	Mean wind speed \bar{u} (m s^{-1})	Mean wind direction $\bar{\theta}$	σ_u/\bar{u}	σ_θ	Re_*	Fetch	Atmospheric stability z'/L	Averaging time (min)	Sampling frequency (Hz)
COSMO	0.73	26°	0.59	35.7°	810	40H	-0.15	60 (240T)	30
WT	0.96	0°	0.18	5.8°	68	85H	0	3 (180T)	4

Mean wind speed, wind direction, and atmospheric stability were calculated at a height of $2H$. T is eddy turnover time defined as $T = H/(u_*)_{2H}$

independence can be expected. The experimental conditions of COSMO and the wind tunnel are presented in Table 1. In the table, measurement times were normalized using eddy turnover time $T = H/(u_*)_{2H}$. The standard deviation of θ is $\sigma_\theta = 35.7^\circ$ for COSMO, which is much larger than $\sigma_\theta = 5.8^\circ$ for the wind tunnel.

For the cases of shorter fetch lengths discussed in Sect. 5, building arrays to the upstream side of the measurement section were gradually removed and were replaced by 20 mm high tripping fences. The target section for PIV measurements was fixed through all measurements, so that the centre of the building gap was always positioned at 6.45 m downstream from the entrance of the wind tunnel. The experimental conditions are presented in Table 5 in Sect. 5.

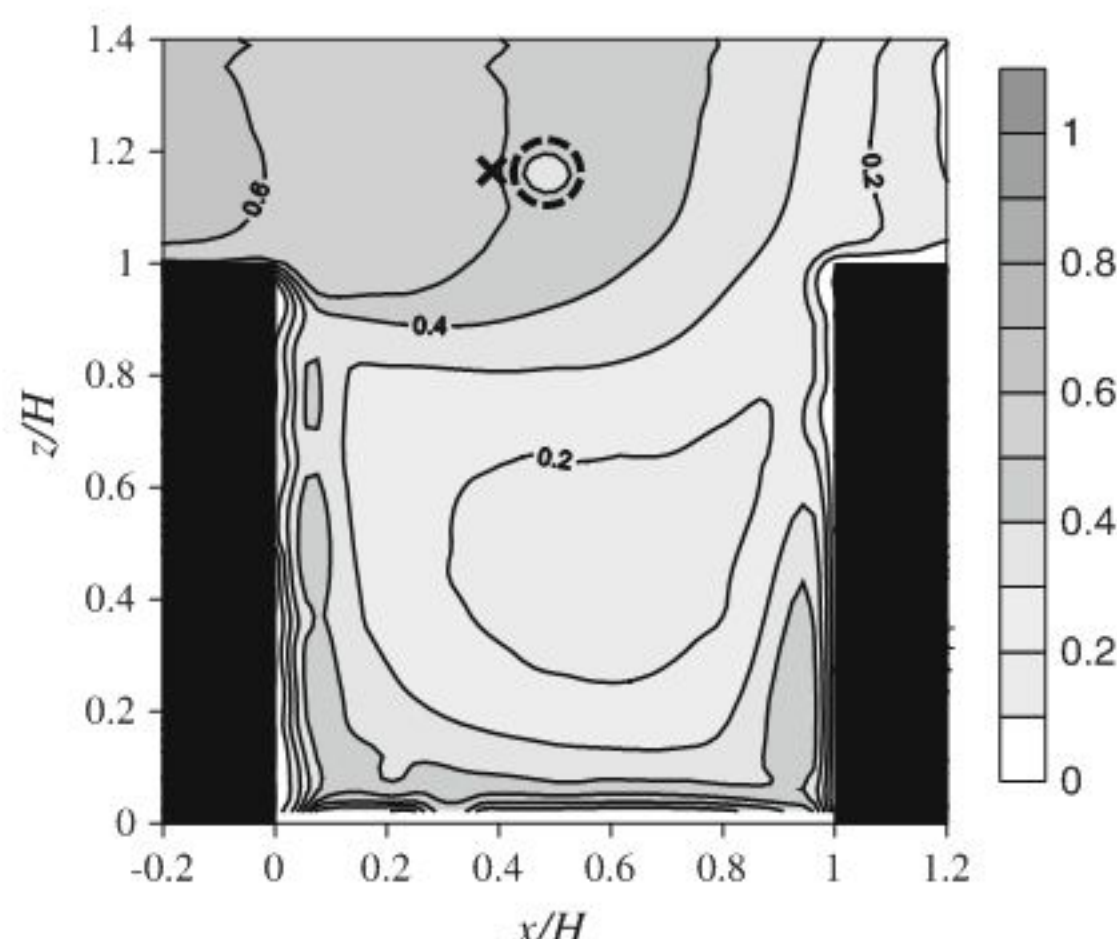
3 Quality of the PIV Dataset in COSMO

Highly fluctuating wind direction and the large-scale building models of the COSMO site made it difficult to supply tracer particles constantly and homogeneously to the measurement section. The lack of tracer particles resulted in the failure of visualization, and led to data deficits of PIV measurements both spatially and temporally. Although it was thought that an additional supply of tracer would solve the problem, it was found that too much tracer smoke added noise to the image analysis. The data acquisition rate (DAR), which is expressed as the fraction of valid data during the measurements, can be calculated for each grid point as

$$d_{i,j} = \frac{1}{N} \sum_{n=1}^N \varepsilon_{i,j}(n). \quad (1)$$

Here, i and j indicate the grid number in x and z coordinates, respectively; N is the total data number ($N = 108000$); and ε is a function that is 1 when valid data are obtained, and zero otherwise. Figure 3 shows the spatial distribution of DAR. The main causes of data deficits are (1) lack of tracer particles, (2) weak contrasts of tracer concentration, and (3) large deformation of tracer concentration between a pair of particle images. The third factor can occur during oblique wind directions or high wind speed. The lower values at the downstream side result from both the first and second factors because of the strong turbulent diffusivity. The lower values at the centre of the cavity are due to the first factor, that is, lower concentrations of particles in this area. Although the lowest DAR is about 16%, the data number is considered to be sufficient to compute statistics considering the large number of N . However, the data deficits are not random but depend on wind direction and wind speed, which could have introduced a bias in the mean statistics. Details of this bias are given later in this section.

Fig. 3 Distribution of data acquisition rate. The *black circle* denotes the position of a sonic anemometer, and the *cross mark* denotes the position of PIV grid data used in the comparison with the sonic



To examine the accuracy of the PIV dataset, wind speed and mean statistics obtained from PIV and the $1.2H$ sonic were compared. The sonic sampling rate was degraded from 50 to 30 Hz for the comparison. Since this sonic was installed inside the measurement section of PIV, it was an obstacle for the analysis of visualized images. Hence, the comparison was done with the PIV dataset of the grid point 0.18 m upstream of the sonic anemometer (cross mark in Fig. 3). Figure 4 shows scatter plots of u and w obtained from PIV and sonic measurements. The correlation coefficient for u components is $R = 0.84$, and points fit well on the line of $y = x$. On the other hand, the plot of vertical velocity w is scattered, and the correlation of PIV and sonic measurements ($R = 0.54$) is weaker than when using horizontal velocity. This relatively weak correlation can be explained as follows. Firstly, the range of the fluctuations in w is smaller than that for the u component, and the PIV measurement error is relatively large for the vertical velocity component. If the sonic data are assumed to represent true values, then the root-mean-square error of the PIV measurements is 0.19 m s^{-1} for u and 0.17 m s^{-1} for w . Here, root-mean-square error was calculated as the square root of $(u_{\text{PIV}} - u_{\text{sonic}})^2$ and $(w_{\text{PIV}} - w_{\text{sonic}})^2$. Secondly, we consider the high spatial variance of vertical velocity. Ganapathisubramani et al. (2005) presented horizontal distributions of the two-point correlation over a flat surface using both u and w components, and revealed that the correlation of vertical velocity decayed much faster than horizontal velocity with increasing distance from a reference point. From the PIV measurements in the wind tunnel (Row43 case), the two-point correlation was calculated at the equivalent locations to those of the sonic anemometer and the compared PIV grid point in COSMO. The correlation coefficients were $R_{uu} = 0.94$ for horizontal velocity, and $R_{ww} = 0.76$ for vertical velocity. The same tendency has also been observed in COSMO (Inagaki et al. 2009). Figure 6 shows the histogram of w obtained from PIV and sonic measurements. The good agreement between them indicates the good reliability of mean statistics from the PIV measurements (Fig. 5).

Turbulence statistics obtained from the PIV and sonic measurements are shown in Table 2. The statistics in the column labelled ‘Sonic#’ were calculated using the sonic data only for the period of valid PIV data, and ‘Sonic’ is for the entire period. The comparison of ‘PIV’ and ‘Sonic#’ shows good agreement in every statistic. However, in the comparison of ‘PIV’ and ‘Sonic’, the friction velocity is obviously underestimated by the PIV measurement. This discrepancy is quantified by the difference between ‘Sonic’ and ‘Sonic#’, and thus indicates the bias introduced by the PIV data deficit. Figure 6 shows the histogram of wind direction,

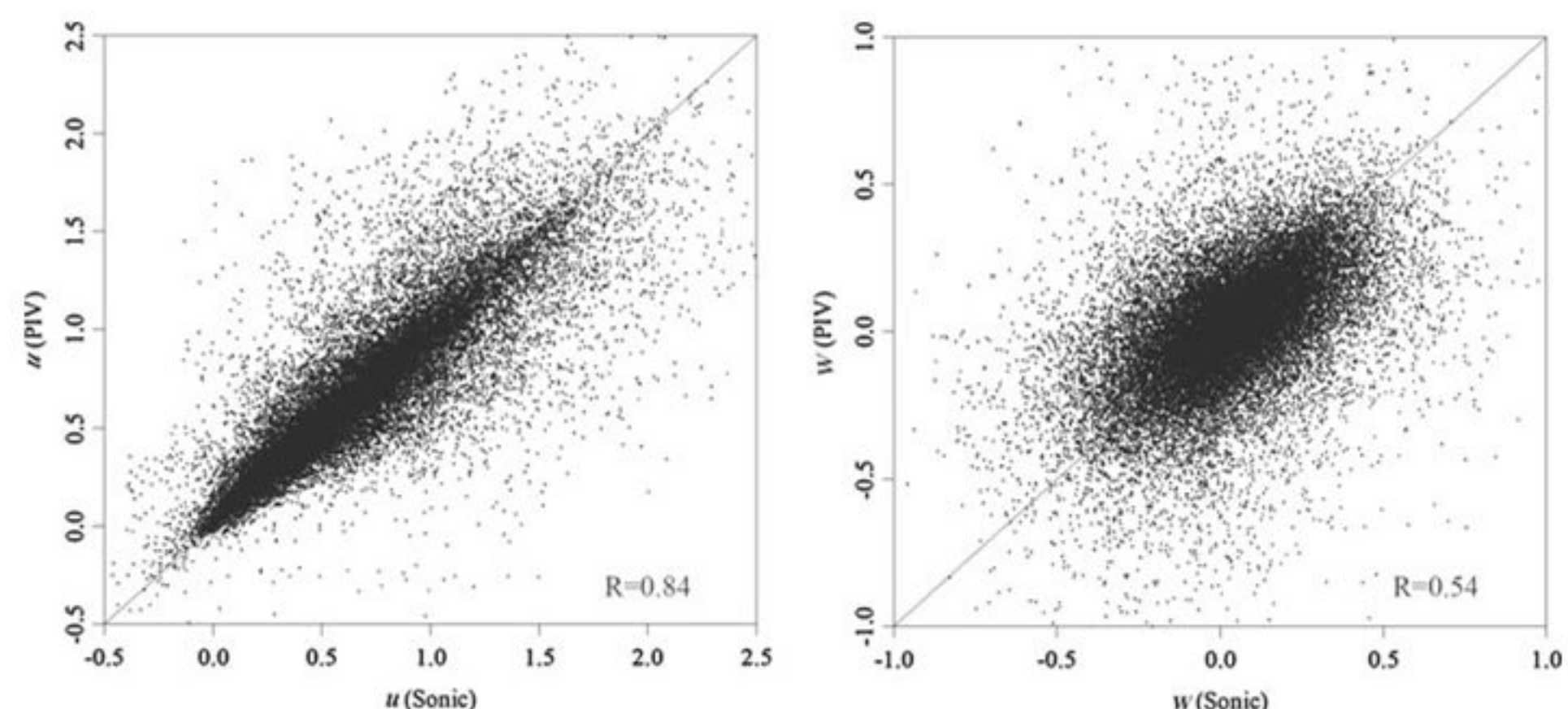


Fig. 4 Scatter plots of u and w obtained from PIV and sonic measurements at the COSMO site

Fig. 5 Histogram of w obtained from PIV and sonic measurements at the COSMO site

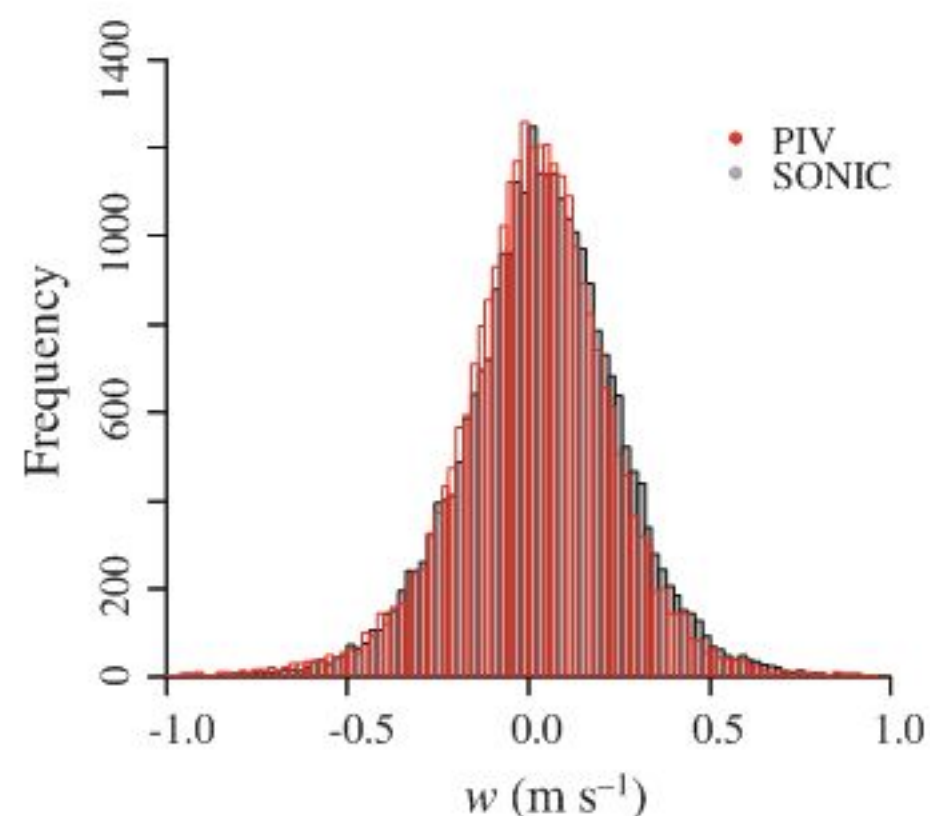


Table 2 Comparison of the mean statistics between the PIV and Sonic datasets

	PIV (m s^{-1})	Sonic# (m s^{-1})	Sonic (m s^{-1})	PIV/Sonic#	PIV/Sonic
\bar{u}	0.67	0.67	0.65	1.00	1.02
σ_u	0.37	0.38	0.38	0.97	0.98
σ_w	0.19	0.18	0.20	1.05	0.95
u^*	0.12	0.12	0.15	1.04	0.83

The statistics in the column labelled ‘Sonic#’ were calculated by ignoring the sonic data during the time of the PIV data deficits, and ‘Sonic’ was for the entire period

streamwise velocity and vertical velocity. The solid and broken lines represent the DAR for the period of each frequency bin at heights of $1.2H$ (the position used for comparison with sonic) and $0.5H$, respectively. From Fig. 6a, it is found that DAR decreases with oblique wind direction. This is due to a smaller amount of tracer particles from seeding devices reaching the measurement section, and the larger deformation of the tracer concentration patterns at

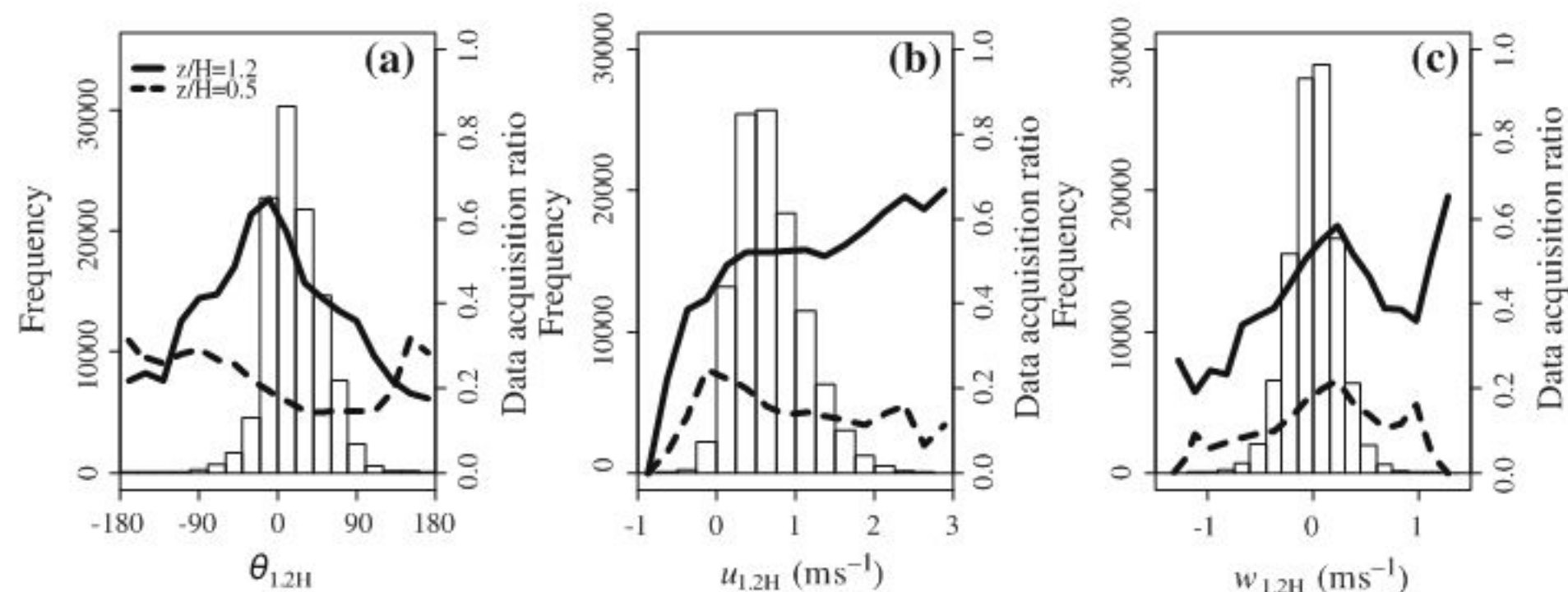


Fig. 6 Frequency distributions for **a** wind direction, **b** streamwise velocity, **c** vertical velocity at the COSMO site. *Solid line* represents the data acquisition ratio for each frequency bin at $(x/H, z/H) = (0.38, 1.2)$ (*right axis*). *Dashed line* is same as solid line but for $(x/H, z/H) = (0.5, 0.5)$

the laser sheet. Since the COSMO site has regular alignment, the frontal area index of this site depends on wind direction, and the largest frontal area index is obtained at $\theta = 45^\circ$. Kanda et al. (2007) reported that the roughness length z_0 depends on wind direction for COSMO, and z_0 in the case of $\bar{\theta} = 45^\circ$ is nearly twice that for the case of $\bar{\theta} = 0^\circ$. This implies that when θ becomes large, DAR decreases, and the conditions with large momentum flux will be undersampled. This explains why the friction velocity was underestimated in the field PIV. However, the DAR at $0.5H$ does not depend on the wind direction. The seeding devices installed in the canopy, and the relatively low wind speed, seem to minimize the dependency on wind direction. In contrast to wind direction, DAR does not depend much on u for both $z = 1.2H$ and $z = 0.5H$ except for the period of $u < 0$ (Fig. 6b). The slight increase in DAR with increasing u is because of the correlation between u and θ . The dependence on vertical velocity is large as presented in Fig. 6c, the larger magnitude of vertical velocity leading to the smaller DAR.

To confirm the biases generated from the data deficits, weighted averages were calculated by the following procedure. Firstly, each vector map was labelled according to the wind direction, the streamwise velocity and the vertical velocity measured by the $1.2H$ sonic. Table 3 shows the classifications of $|\theta|$, u , and w . Each parameter has four, two and three bins, respectively, and finally each vector map was divided into 24 groups by the combinations of these classifications. Then, turbulence statistics for each grid point were calculated from

$$\bar{\phi}_{\text{wa}} = \frac{1}{N} \sum_{\alpha=1}^4 \sum_{\beta=1}^2 \sum_{\gamma=1}^3 \langle \phi_{\alpha,\beta,\gamma} \rangle N_{\alpha,\beta,\gamma}, \quad (2)$$

where, the subscript wa indicates weighted-average, α, β, γ are the labels shown in Table 3, and $N_{\alpha,\beta,\gamma}$ represents the number of vector maps in each group. $\langle \phi_{\alpha,\beta,\gamma} \rangle$ is the ensemble-averaged value for each group, which can be expressed as

$$\langle \phi_{\alpha,\beta,\gamma} \rangle = \frac{1}{\sum_{n=1}^{N_{\alpha,\beta,\gamma}} \varepsilon_{\alpha,\beta,\gamma}(n)} \sum_{n=1}^{N_{\alpha,\beta,\gamma}} (\phi_{\alpha,\beta,\gamma}(n) \cdot \varepsilon_{\alpha,\beta,\gamma}(n)). \quad (3)$$

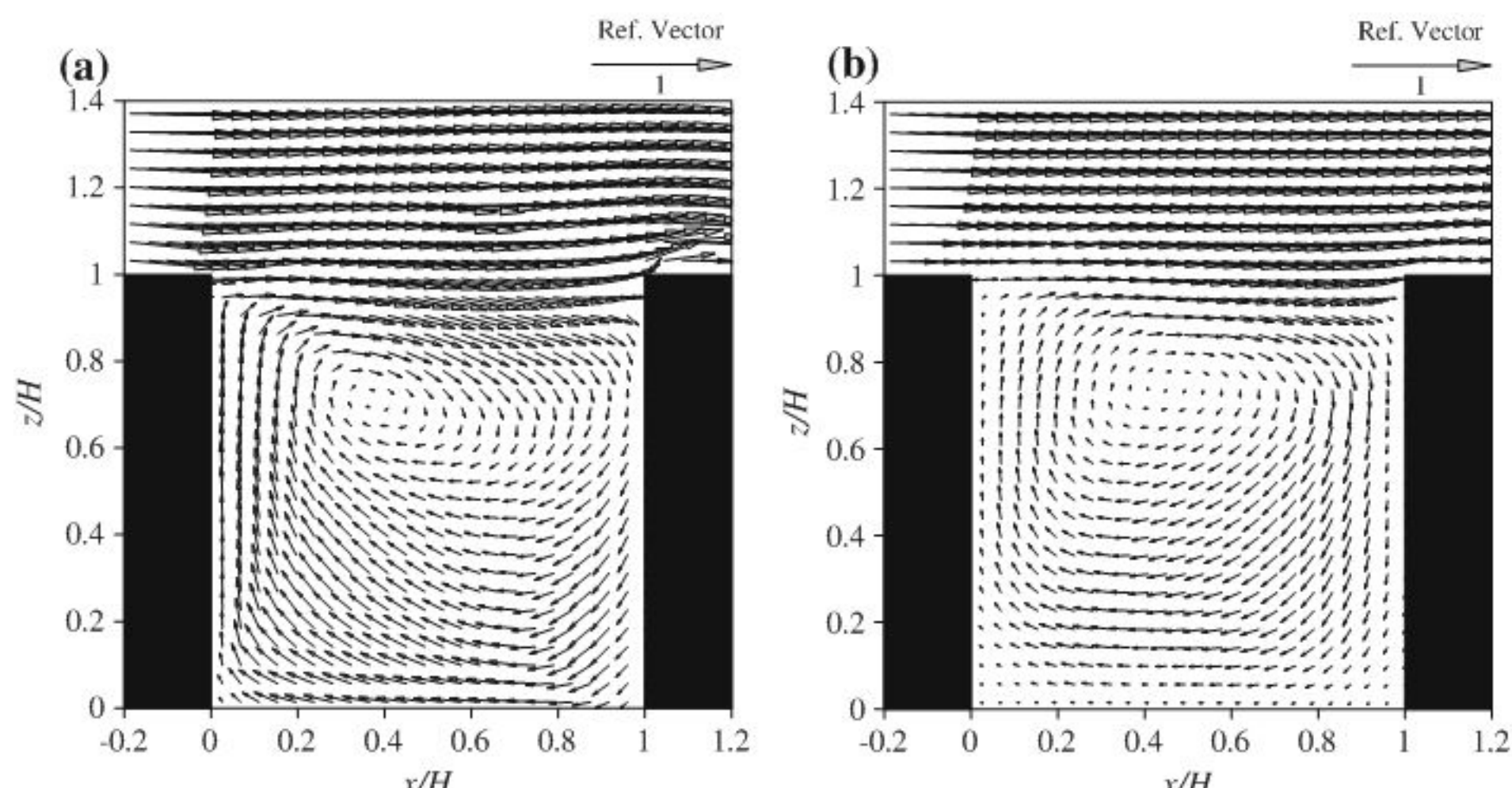
If the DAR was unity at every grid point, then $\bar{\phi}_{\text{wa}}$ would be equivalent to the usual temporal average. The concept of this weighted averaging is to treat the data of every group

Table 3 Classification of $|\theta|$, u , and w for weighted-averages

	$ \theta $		u		w
$\alpha = 1$	$ \theta \leq 5^\circ$	$\beta = 1$	$u \leq 0$	$\gamma = 1$	$w \leq -0.2 \text{ ms}^{-1}$
2	$5^\circ < \theta \leq 15^\circ$	2	$u > 0$	2	$-0.2 \text{ ms}^{-1} < w \leq 0.2 \text{ ms}^{-1}$
3	$15^\circ < \theta \leq 45^\circ$			3	$0.2 \text{ ms}^{-1} < w$
4	$45^\circ < \theta $				

Table 4 Weighted-averaged PIV statistics and their comparison with the Sonic

	PIV _{wa} (ms^{-1})	Sonic (ms^{-1})	PIV _{wa} /Sonic
\bar{u}	0.65	0.65	1.00
σ_u	0.38	0.38	1.01
σ_w	0.19	0.20	0.98
u^*	0.14	0.15	0.91

**Fig. 7** Mean vectors normalized with \bar{u}_{2H} : **a** COSMO, **b** wind tunnel

fairly regardless of the value of DAR, assuming that $\langle \phi_{\alpha,\beta,\gamma} \rangle$ is a representative value of each group. By comparing the weighted- with temporal-averaged statistics, the differences of the magnitudes in Reynolds stress and variances are found to be up to 10–20%, but there is no significant change in their spatial distributions (not shown). Table 4 shows the statistics after weighted averaging, and each PIV statistic becomes closer to the value of ‘Sonic’. Hence, the weighted-averaged statistics are used for Figs. 7 and 9. Since the DAR is almost 100% in the wind-tunnel experiments, weighted averaging is not applied to the wind-tunnel measurements.

4 Mean Flow Statistics

Figure 7 shows the mean vector maps for COSMO and the wind tunnel normalized with \bar{u}_{2H} . Both flow patterns have one cavity circulation in the building gap, but the circulation is stronger in the COSMO case especially at the roof level. Vectors in the lower part of the gap also show different features such as the dominance of downward vectors in the wind tunnel and upward vectors in COSMO. The location of the circulation's centre is at $x = 0.37H$ for COSMO and at $x = 0.46H$ for the wind tunnel. Possible reasons for these differences relate to the different conditions of COSMO and the wind tunnel in (1) mean wind direction and its fluctuation, (2) atmospheric stability, (3) outer-layer disturbance, and (4) Reynolds number. The difference in mean wind direction may have significant effects on the mean flow fields and unsteady motions (Kim and Baik 2004). Reynolds number dependency was examined by changing the free stream velocity of the wind-tunnel experiments from 1 to 3 m s^{-1} . The experiments revealed little difference in the mean flow fields, thereby indicating insignificant effects of Reynolds number differences. Figure 8 shows conditionally-averaged vector maps according to the wind direction measured at $z = 1.2H$ using a threshold of $u_{1.2H} > 0.3\text{ m s}^{-1}$. Figure 8a and b is obtained using conditions of $|\theta| \leq 5^\circ$ and $15^\circ < |\theta| \leq 45^\circ$, respectively. For oblique wind directions (Fig. 8b), downflow at the roof height becomes strong and the circulation's centre is located at $x = 0.33H$, whereas the circulation's centre is located at $x = 0.41H$ for parallel wind directions. This result indicates that the larger inclination, or the fluctuation of wind direction at the COSMO site, is responsible for some different aspects of the mean flow structures in COSMO and the wind tunnel. As previously mentioned, the oblique wind direction leads to a larger momentum flux, which accelerates the inflow to the canopy layer. This intensive downflow can also shift the centre of the cavity vortex to the upstream side. However, the flow near the floor does not change significantly with the change in wind direction. Those stronger upward vectors near the floor in the COSMO measurement were observed consistently for 1 h even with a shorter averaging period, e.g. 5-min average. Hence, disturbances that have a time scale of 5–30 min, such as convective motions,

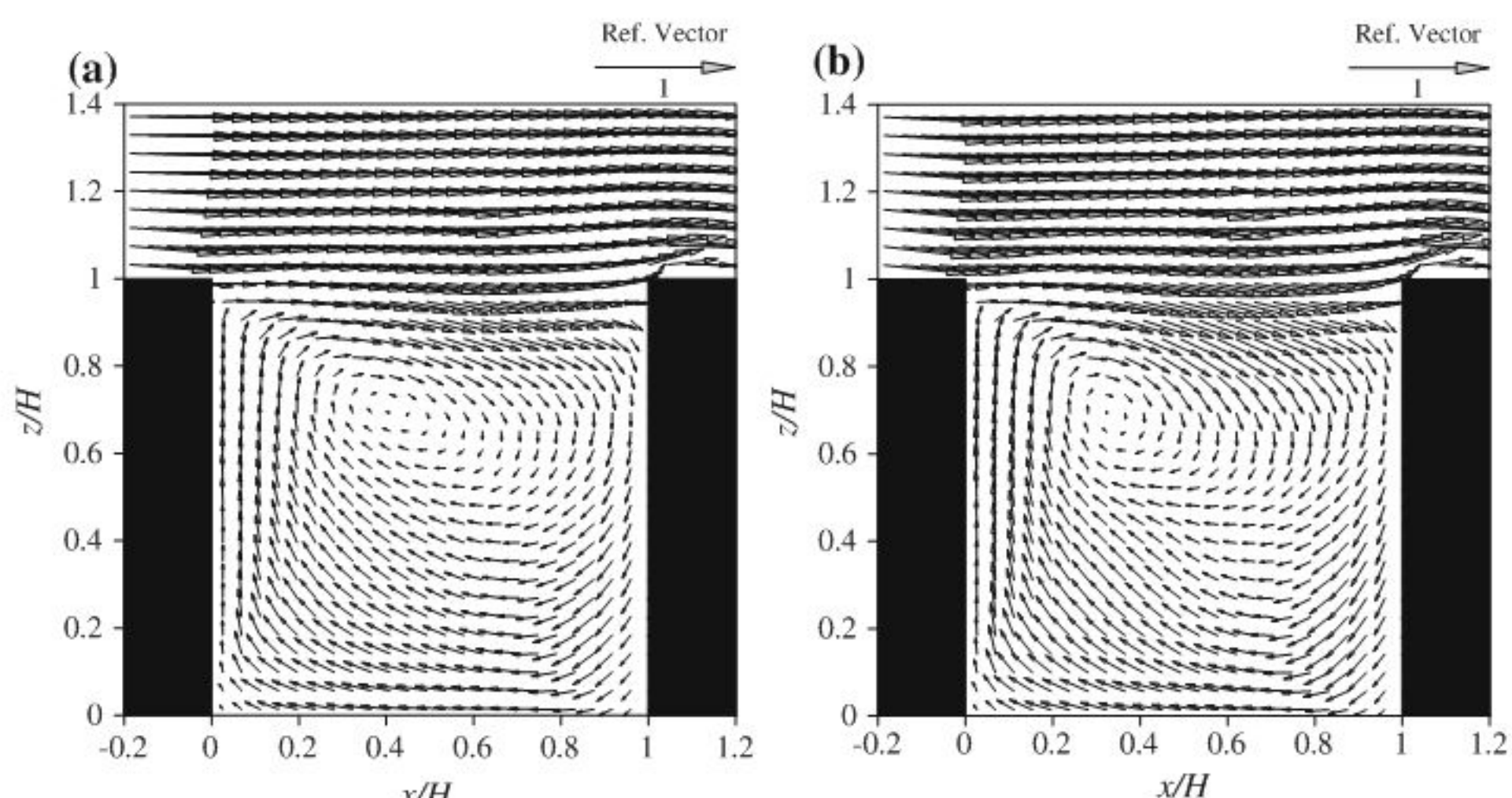


Fig. 8 Conditionally-averaged vector maps (COSMO site): **a** $|\theta| \leq 5^\circ$, **b** $15^\circ < |\theta| \leq 45^\circ$. Vectors are normalized with the ensemble average of u_{2H} for each condition. Only data for the time period of $u_{1.2H} > 0.3\text{ m s}^{-1}$ were employed to exclude weak wind conditions

do not have a significant influence on those upward motions. The one reason for this difference is the moderately unstable conditions in the field measurement. Unstable conditions can aid acceleration of the circulation in canopy layers and the dominant upward flow near the ground (Uehara et al. 2000). Similar differences were also observed in the wind-tunnel experiments between neutral and unstable conditions (Takimoto et al. 2009).

Figure 9a and b is the contour maps of Reynolds stress in the outdoor and the indoor canopies normalized with friction velocity $u_* = \sqrt{-(\bar{u}'\bar{w}')_{2H}}$. The large values of momentum fluxes are found mostly in the upper region of the building gap in COSMO, whereas the position of the maximum momentum flux was shifted to the windward wall and shows a narrower peak in the wind-tunnel data. This wider peak in the field measurement is considered to be a result of larger fluctuations in wind direction at the COSMO site, and this is confirmed by the conditional average of Reynolds stress filtered by the same conditions as Fig. 8 (not shown). The distributions of the standard deviation of u presented in Fig. 9c and d show that σ_u above the canopy layer is much higher for COSMO. This large value above the canopy layer is due to the outer-layer disturbances that increase temporal fluctuations. In contrast, the value of σ_u inside the canopy shows similar magnitudes, i.e. the influences of the outer-layer fluctuations are small. Figure 9e and f shows the standard deviation of w —although the distributions of σ_w are different for COSMO and the wind tunnel, the region of large values corresponds to the strong downward flow near the downstream block. The magnitude of vertical wind speed is large in the region of strong downdrafts, and the downflow is directly connected to the flow above the canopy layer. As a result, the value of σ_w is large in the regions of strong downflow, and the different characteristics of the distribution of σ_w are due to the difference in the mean flow structures in COSMO and the wind tunnel.

5 Instantaneous Flow Structures

5.1 Shear-Layer Dynamics

The shear layer formed by the rapid deceleration of the wind at roof levels is said to fluctuate vertically, and the ‘flapping’ of the shear layer controls the strength of the flow in streets (Louka et al. 2000). Figure 10 shows examples of instantaneous flow structures obtained at the COSMO site along with the magnitude of spanwise vorticity. In these figures, vortex sheets, i.e. shear layers, were successfully visualized, and they revealed flapping motions around the canopy top. An example of downward penetration of the shear layer is shown in Fig. 10a, while Fig. 10b shows another pattern of the shear layer where it is tilted upwards because of the upward flow from the canopy layer. To check the connections between these patterns of vortex sheets and the flow field, ensemble averages of the vorticity fields were made for both the sweep mode ($u' > 0, w' < 0$) and the ejection mode ($u' < 0, w' > 0$) and are shown in Fig. 11. Here, the mode of each flow field was determined using the $1.2H$ sonic anemometer, and a threshold of $|u'w'|_{1.2H} \geq |\bar{u}'\bar{w}'|_{1.2H}$ was utilized to exclude ambiguous events. For the sweep mode, the shear layer is near the upstream block, and it descends towards the canopy layer. It can be conjectured that the downward pattern of the shear layer is related to the sweep motion that shifts the velocity gradient at the roof surface and creates downflow at the canopy top. Although the ejection mode has a similar shear layer at the roof top, the intensity is much weaker than for the sweep mode. The shear layer appears to be lifted up in Fig. 11b (red circle), but it is insufficiently clear to indicate the influence of ejection flow on the formation of an uplifting shear layer. In fact, these upward patterns of the

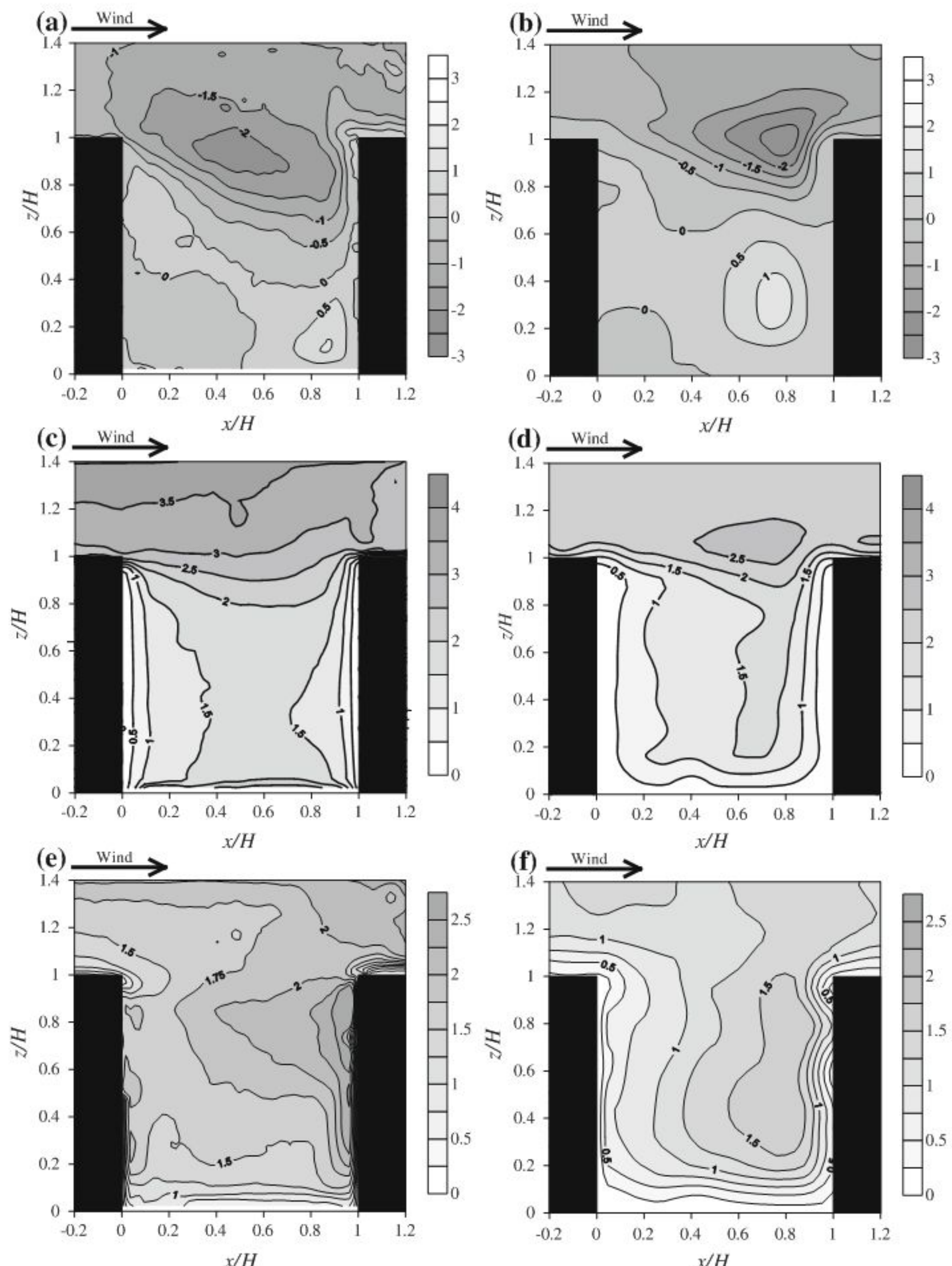


Fig. 9 Spatial distribution of turbulence statistics: **a** and **b** are turbulent momentum flux $\overline{u'w'}/u_*^2$, **c** and **d** are the standard deviation of u , **e** and **f** are the standard deviation of w . **a**, **c**, **e** are for COSMO, and **b**, **d**, **f** are for the wind tunnel. All statistics are normalized with friction velocity obtained at $z = 2H$

shear layer were often observed with updrafts from the canopy layer as exhibited in Fig. 10b rather than the ejection flow, since the ejection flow often weakened the velocity gradient at the roof surface.

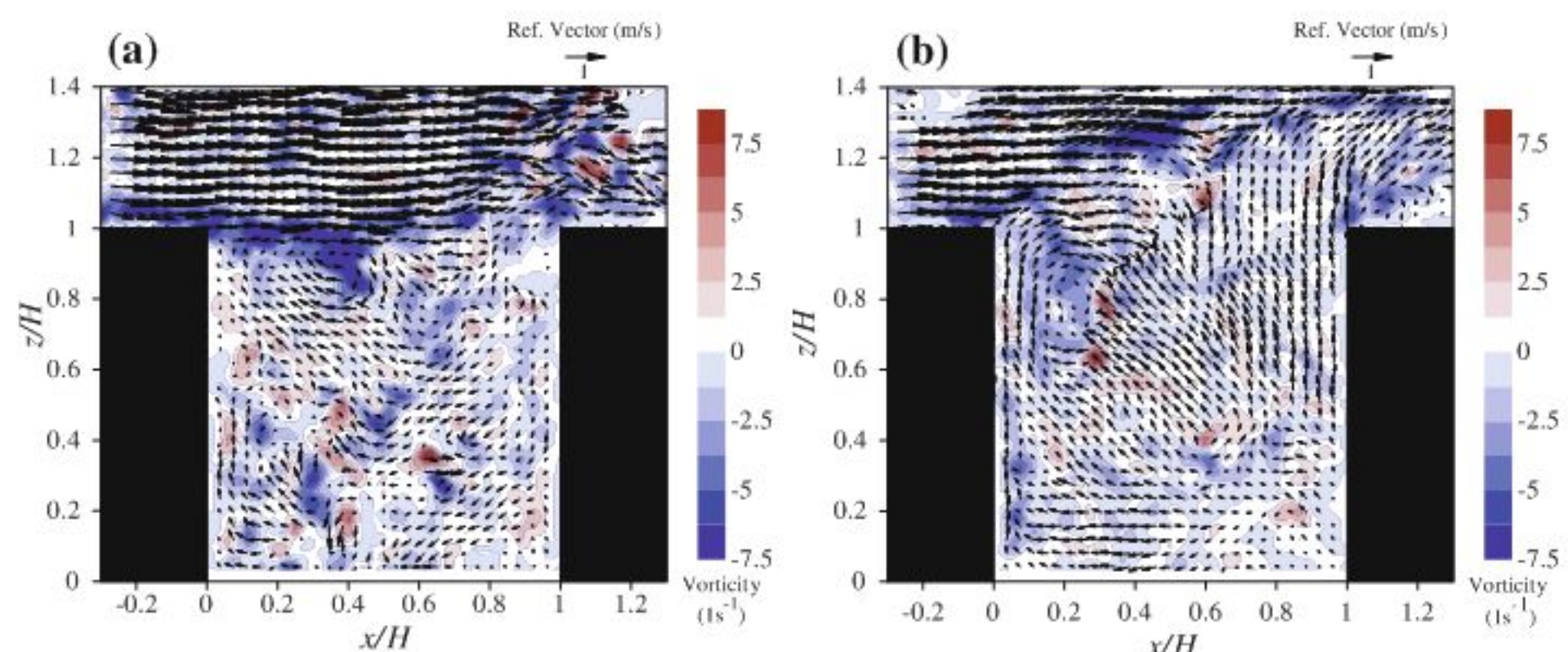


Fig. 10 Instantaneous flow structures with out-of-plane vorticity at COSMO: **a** downward shear layer, **b** upward shear layer

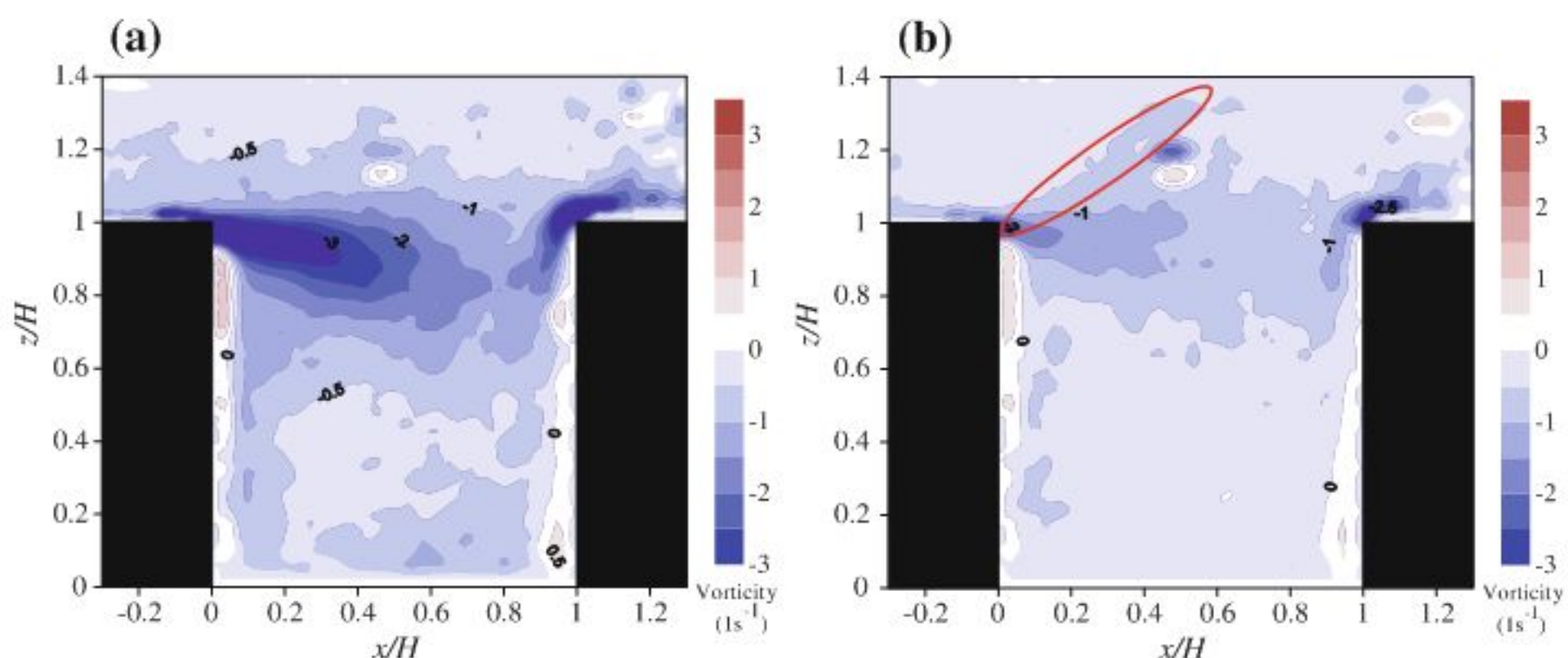


Fig. 11 Ensemble average of vorticity fields for the time of **a** sweep mode, **b** ejection mode (COSMO). Mode of each flow field was determined by using the $1.2H$ sonic anemometer, and a threshold of $|u'w'_{1.2H}| \geq |u'w'_{1.2H}|$ was used. The *red ellipse* indicates the lifting up of the shear layer

5.2 Flushing Motions

Apart from the fluctuation of the shear layer, the PIV measurements reveal complex and widely varied instantaneous flow structures in canopy layers. The position of the centre of the cavity circulation tended to be located within the upper half of the cavity, but it ranged from the upstream side to the downstream side and, occasionally was even in the lower half of the cavity. There were also periods exhibiting multiple eddies inside the cavity; sometimes there was no circulation at all, and the flow was dominated by lateral convergence. Among those flow regimes, this subsection deals with the so-called flushing motions shown in Fig. 12. Flushing is characterized by large-scale upward motion that is distinctively different from the usual cavity eddy in which scalars are often trapped (Walton and Cheng 2002). During these upward motions, tracer particles were flushed out from the canopy layer. Although the concentration of tracer particles was not measured, the considerable contribution of the flushing phenomenon to scalar transport has been confirmed by numerical simulations: Inagaki et al. (2010) indicated that flushing motions entail the horizontal convergence of air flow near the

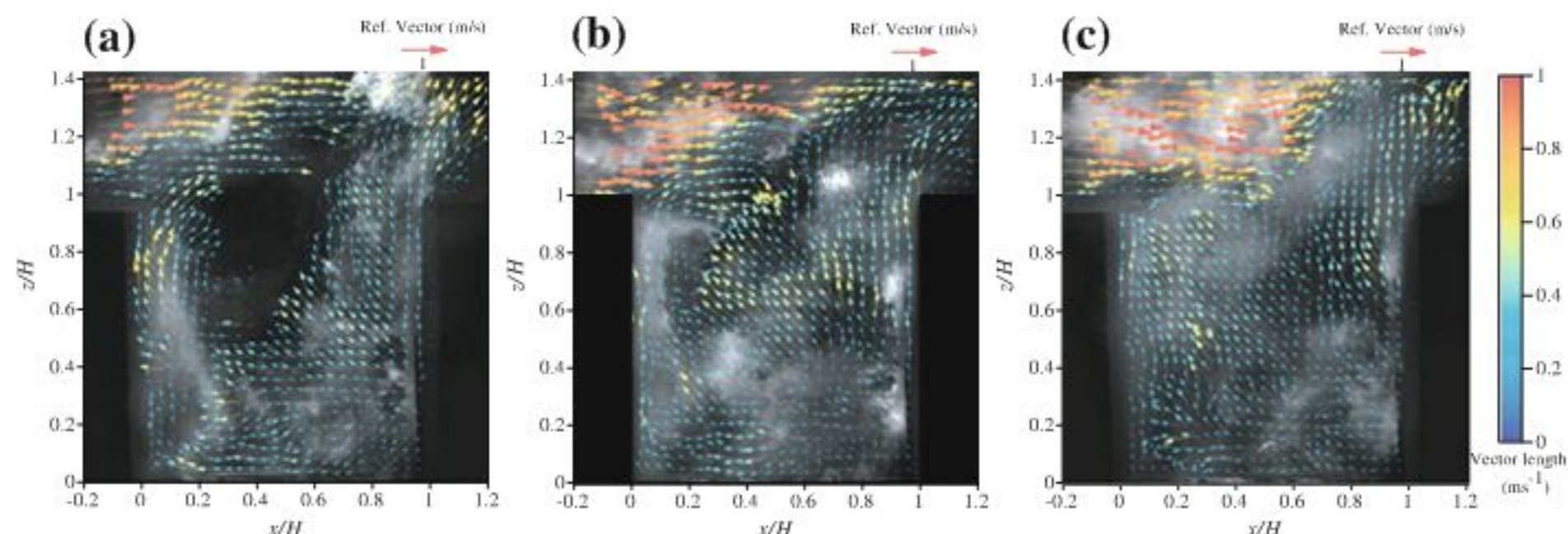


Fig. 12 Flushing motions observed at COSMO. The interval of each snapshot is 1 s, and the timeline is from left to right

ground, whereby the heat flux out of the canopy layer is nearly three times larger than the mean heat flux at the top of the building gaps.

To examine the general aspects of flushing in the experiments, the ensemble average was taken by defining flushing events from the vector maps where valid vectors were obtained at more than 75% of grid points inside the canopy ($0 < x/H < 1$, $0 < z/H < 1$). For the objective algorithm, the following criterion, ‘more than α % of valid vectors satisfy the condition of $w > |u|$ inside the canopy’, was applied. This condition first specifies significant upflow vectors by the threshold of ‘ $w > |u|$ ’, and then the value of α indicates the spatial extent of the upward flow. Owing to the two-dimensional nature of the PIV dataset, spanwise velocity components were not taken into account. The value of $\alpha = 55$ was adopted as this gave the most agreeable results with manual detection. As a result, 5,463 vector maps were sampled, and 354 of them were identified as flushing phenomena. Figure 13a shows the ensemble-averaged flow field for flushing events. Only the vectors in the lower part of the cavity show backward flow rather than upflow, which is dominant in the layer above. The upflow around a height of $z = 0.7H$ is especially prominent, and becomes weaker at the canopy top. The wind speed above the canopy layer is lower than the temporal average, and the ejection mode is found to be dominant. Figure 13b is the ensemble average of the turbulent momentum flux during flushing events. The value of $\langle u'w' \rangle / u_*^2$ at the canopy top is almost four times larger than the values shown in Fig. 9a. Although the time fraction of flushing was limited in the current experiment, this phenomenon appears to lead to efficient momentum and scalar exchanges in urban canopy layers associated with a remarkable release of scalars from the canopy layer. Judging from the vector maps and raw particle images, the frequency of flushing was estimated to be once in 2–3 min, and their duration times were mostly 2–5 s. Therefore, the time fraction of flushing motion was about 3%, and the stress fraction was estimated to be around 12% at the canopy top.

Similar flushing events were also observed in the wind-tunnel measurements. Therefore, flushing motions are generated by the disturbances of the internal boundary layer rather than thermal buoyancy or outer-layer disturbances. Hereafter, the wind-tunnel data are employed to simplify the issues and examine the conditions of the flow field during flushing events. Since the sampling frequency of the wind-tunnel measurements was limited to 4 Hz, many of the flushing events extracted by the above criterion were observed only in one snapshot with little correlation to the previous or the subsequent snapshots. It is difficult to estimate the duration of flushing motions precisely, but occasionally they were observed in two to four consecutive snapshots. Hence, their mean duration time is estimated to be 0.25 s or somewhat

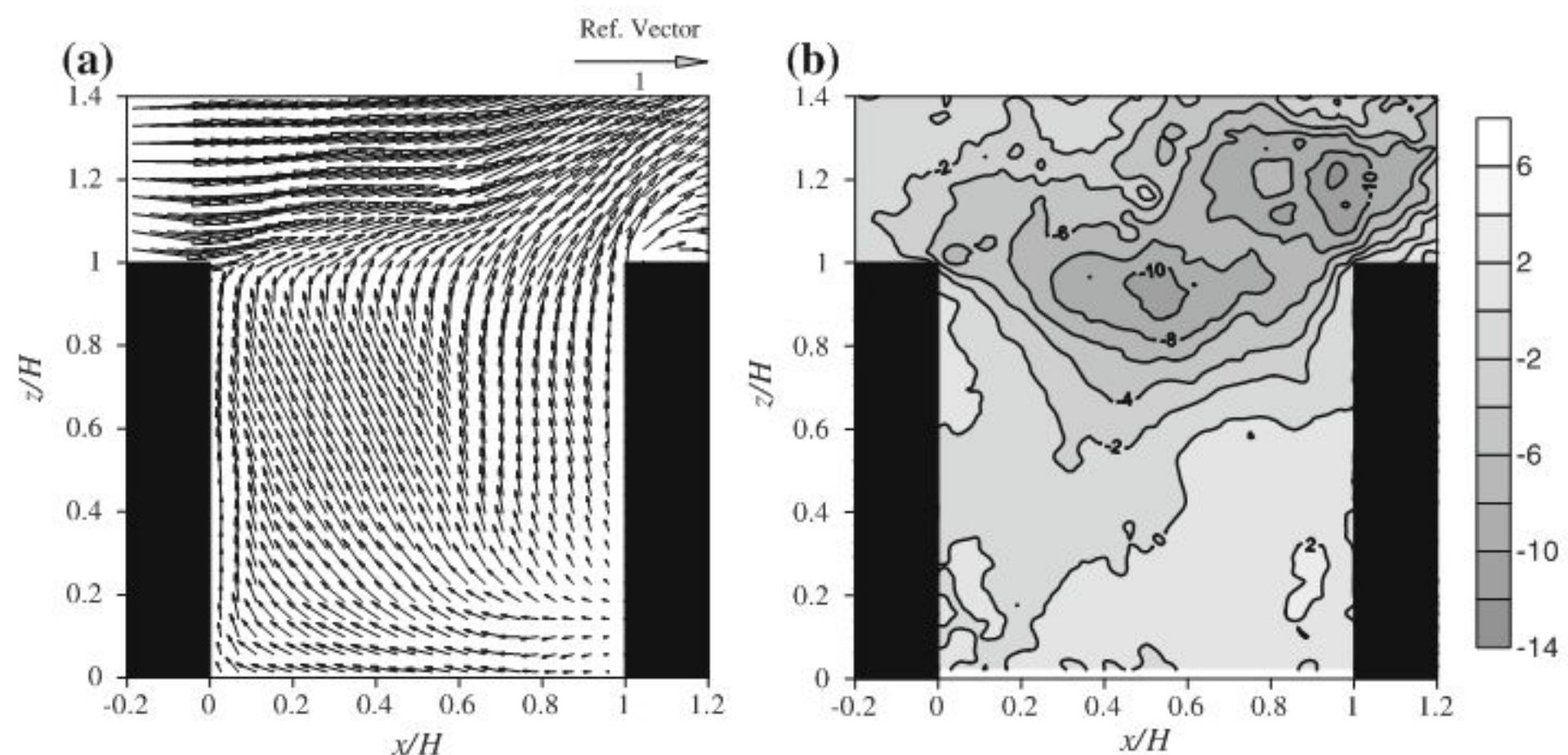


Fig. 13 Ensemble average of flushing events at the COSMO site: **a** wind velocity map normalized with \bar{u}_{2H} , **b** turbulent momentum flux $\langle u'w' \rangle / u_*^2$

longer than that. If the events were observed in consecutive snapshots, then they were counted as one event. As a result, 13 flushing events were observed in a 3-min measurement period for the Row43 case, which was used in comparison with COSMO data. It is noted that flushing events could be undersampled because of the coarse sampling interval of the measurements.

In addition to the Row43 case, a series of experiments was conducted by changing the fetch upwind of the building array. Table 5 shows the experimental conditions of each measurement case. The integral length scale shown in Table 5 was calculated from Eq. (4) using the temporal fluctuation of u measured by the LDA at a height of $1.4H$. The turbulence intensity at this height is less than 0.5 in every case, thereby allowing the use of Taylor's hypothesis.

$$L_u = \frac{\bar{u}}{\sigma_u} \int_0^\infty \overline{u'(t)u'(t+\tau)} d\tau. \quad (4)$$

The same criterion ($\alpha = 55\%$) of flushing events was applied to these cases, and the numbers of detected events are presented in Table 5. From this result, the frequency of occurrence of flushing events is found to increase as the fetch increases. In particular, no flushing events were observed for the case of Row1 and Row2. The ensemble average of 79 snapshots of flushing events obtained from each measurement case is very similar to the flushing motions in the COSMO site (not shown). Figure 14 shows sample snapshots of a flushing event that lasted for four consecutive vector maps. Blue colour vectors represent low-speed vectors that have a lower streamwise velocity than the local temporal mean. Low-speed vectors are dominant above the canopy layer throughout the event, and have a coherent structure. Kanda (2006) exhibited the presence of the streaky structures of low-momentum region over cubic arrays whose streamwise length scale is about ten times larger than the cube height. This is a common structure developed above urban canopy layers, and its structure resembles the low-speed streak over smooth surfaces (e.g. Jeong et al. 1997). In flat boundary layers, low-speed streaks are often generated with packets of hairpin vortices (Zhou et al. 1999), and involve ejection flows inside their structure. It has not been determined if this model is applicable to rough surfaces, but Coceal et al. (2007) visualized similar hairpin-like

Table 5 Conditions of the wind-tunnel experiments

Case	$U_{2H}(\text{ms}^{-1})$	Fetch (H)	Position of trips (m)	Number of flushing events	Integral length scale L_u/H
Row1	1.04	1	0, 1, 2, 3, 4	0	1.4
Row2	1.02	3	0, 1, 2, 3, 4	0	2.2
Row3	1.02	5	0, 1, 2, 3, 4	4	2.3
Row5	1.01	9	0, 1, 2, 3, 4	7	2.9
Row7	0.95	13	0, 1, 2, 3, 4	11	3.7
Row11	0.91	21	0, 1, 2, 3, 4	9	3.7
Row23	0.92	45	0, 1, 2	12	4.9
Row33	0.92	65	0, 1	12	4.8
Row43	0.96	85	—	13	5.0

The measurement time was 3 min for every case. The positions of tripping fences are given relative to the entrance of the wind-tunnel. Integral length scale was calculated at a height of $1.4H$ using the streamwise velocity u

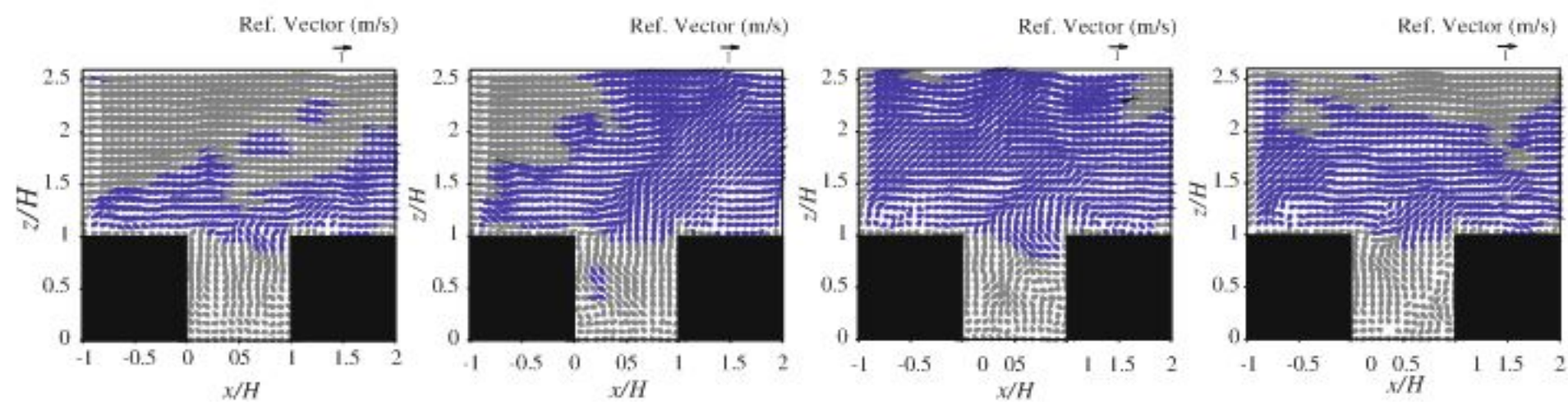


Fig. 14 Four consecutive snapshots of flushing events in the wind tunnel. The interval of each snapshot is 0.25 s, and the timeline is right to left. Blue vectors represent speeds lower than the local temporal mean

vortex tubes around large-scale low-momentum regions over cubic arrays. The presence of the strong upward flow inside the organized structure is also similar to smooth surfaces (Coceal et al. 2007; Inagaki and Kanda 2010), and this upflow may be the driving force for flushing motions inside canopy layers. The scale of the coherent structure in Fig. 14 is about $13H$ applying Taylor's hypothesis, and its shape is similar to the low-speed streaks presented by Kanda (2006), thus, they may be recognized as the same turbulence structures. Assuming that large-scale and coherent structures of low-speed vectors ($u < \bar{u}$) can be classified as low-speed streaks, almost half of the flushing events were observed at the same time as low-speed streaks, even though their time fraction is less than 10%. Here, low-speed streaks were specified using the following threshold that the fraction of low-speed vectors is more than 90% in the area of $-1 < x/H < 2, 1 < z/H < 2$.

The snapshots shown in Fig. 15 are obtained from the Row43 and the Row1 cases, and the mean velocity is subtracted from each vector to display the fluctuating component (blue colour represents ejection mode, and red colour represents sweep mode). In Fig. 15a, flushing can be seen in the canopy with large-scale ejection flow above it. In contrast to this, Fig. 15b exhibits intensive ejection flow only just above the canopy top, and flushing motion did not occur in the canopy. These snapshots are not unique scenes but a general trend as indicated by the integral length scales shown in Table 5. The eddy scale is small in short fetch cases, and the large-scale low-momentum regions are rarely observed. Organized structures seem to require a certain length of building array to be fully developed as the boundary layer

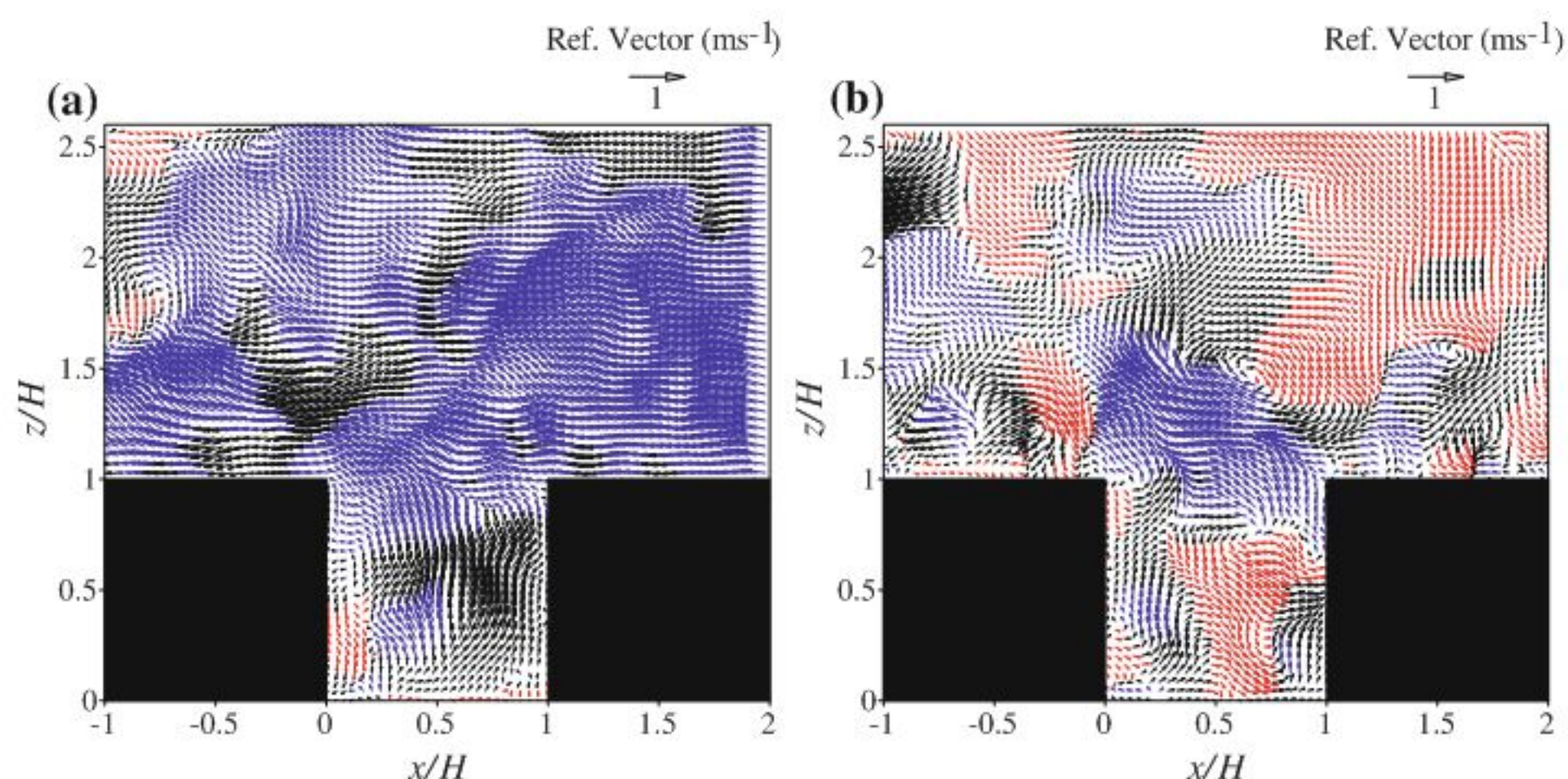


Fig. 15 Instantaneous flow structures in **a** Row43 case, **b** Row1 case. Local mean velocity components were subtracted from each vector. The *blue*, *red*, and *black* colours represent the ejection mode ($u' < 0, w' > 0$), the sweep mode ($u' > 0, w' < 0$), and the other mode ($u' > 0, w' > 0$ or $u' < 0, w' < 0$), respectively

develops. If this large-scale low-momentum region or low-speed streak is an important factor for the generation of flushing, the fetch dependency of low-speed streaks can explain the less frequent flushing events in the shorter fetch case.

However, the observed duration time of most of the flushing events is at least 0.25 s, which is equivalent to $0.25T$ in the Row43 case, and it is smaller than the time scale of low-speed streaks ($10H/\bar{u}_{2H} = 0.75T$). The flushing events in COSMO also have a short time scale of 2–5 s (= 0.13–0.33T), a possible reason being the meandering property of organized structures (e.g. Inagaki and Kanda 2010). The longitudinal axes of low-speed streaks are usually not straight, and our measurements were made only for one vertical cross-section of a building gap. Hence, the length scales of observed organized structures may be smaller than in reality, which would lead to the limited observed time scale of flushing phenomena. Furthermore, the fact that some flushing events were observed without any low-momentum-region structures suggests that organized structures are not an essential requirement for the generation of flushing.

The presence of the opposite flow pattern to the flushing phenomenon, i.e. large-scale downward motion, was also examined. However, there was no clear sign of such flows in both the field and the wind-tunnel measurements. Even if there is impingement of a strong downflow onto the canopy layer, the blocking effect of the roof and the floor diverts the downflow momentum from the vertical to the horizontal (Högström et al. 2002), and tending to generate shear layers at the roof surface or intense cavity circulations, rather than remaining downflow-dominant flow patterns.

6 Concluding Remarks

In this study, a PIV system for observing atmospheric turbulence over an outdoor urban scale model was developed. This system was used for a 60-min-long continuous measurement, and flow structures inside the urban canopy were successfully observed at high spatial resolution. The accuracy of turbulence statistics was favourable in comparison with a sonic anemometer.

Although the inevitable data deficits in outdoor PIV measurements caused a certain degree of bias to the statistics, they were improved by introducing a weighted-average method, and the errors in mean statistics became less than 10%.

The mean flow fields obtained from the outdoor and the indoor measurements revealed different characteristics. These differences can be explained as due to the consideration of only the inclination of wind direction and atmospheric stability, and the impacts of long-period, outer-layer disturbances on the mean flow structures and Reynolds stress being found to be small. However, it must be noted that the standard deviation of wind direction in the outdoor measurement was six times larger than that of the wind-tunnel measurement. It is suggested that we take into account this widely ranging wind direction in the atmospheric environment when flow is modelled in numerical simulations or laboratory experiments.

In the examination of instantaneous flow structures, strong and large-scale upward motions from a building gap were observed both in COSMO and the wind tunnel. These flushing phenomena have a large momentum flux at the canopy top, and are expected to make a contribution to the ventilation inside canopies. From the snapshots taken in the wind-tunnel measurements, their occurrence was found to be correlated with the presence of low-speed organized structures developed over the building arrays. This result suggests that the improvement of the environment in urban canopy layers depends not only on the local surface geometry but can be affected by the organized structures developed in internal boundary layers. Currently, the knowledge of the connections between canopy flow and organized structures is very limited. PIV measurements have a great potential to investigate such interactions, and additional experiments are possibly necessary, such as PIV measurements in horizontal sections and over various types of surface geometries. In addition, three-dimensional flow information is indispensable toward further understanding of this issue, and hence numerical experiments are also required.

Acknowledgments The authors are grateful to Mr. Junnichi Hoshi for his technical support in the wind-tunnel experiments. This research was financially supported by a Grant-in Aid for the Scientific Research (18360234) from Japan Society for the Promotion of Science and by a Grant-in-Aid for JSPS Fellows.

References

- Adrian RJ, Meinhart CD, Tomkins CD (2000) Vortex organization in the outer region of the turbulent boundary layer. *J Fluid Mech* 422:1–54
- Brown MJ, Lawson RE Jr, Decroix DS, Lee RL (2000) Mean flow and turbulence measurements around a 2-D array of buildings in a wind tunnel. In: 11th joint AMS/AWMA conference on the applications of air pollution meteorology. Long Beach, CA
- Cheng H, Castro IP (2002) Near wall flow over urban-like roughness. *Boundary-Layer Meteorol* 104:229–259
- Coceal O, Dobre A, Thomas TG, Belcher SE (2007) Structure of turbulent flow over regular arrays of cubical roughness. *J Fluid Mech* 589:375–409
- Eliasson I, Offerle B, Grimmond CSB, Lindqvist S (2006) Wind fields and turbulence statistics in an urban street canyon. *Atmos Environ* 40:1–16
- Ganapathisubramani B, Hutchins N, Hambleton WT, Longmire EK, Marusic I (2005) Investigation of large-scale coherence in a turbulent boundarylayer using two-point correlations. *J Fluid Mech* 524:57–80
- Högström U, Hunt JCR, Smedman A (2002) Theory and measurements for turbulence spectra and variances in the atmospheric neutral surface Layer. *Boundary-Layer Meteorol* 103:101–124
- Hwang JY, Yang KS (2004) Numerical study of vertical structures around a wall-mounted cubic obstacle in channel flow. *Phys Fluids* 16:2382–2394
- Inagaki A, Kanda M (2008) Turbulent flow similarity over an array of cubes in near-neutrally stratified atmospheric flow. *J Fluid Mech* 615:101–120
- Inagaki A, Kanda M (2010) Organized structure of active turbulence over an array of cubes within the logarithmic layer of atmospheric flow. *Boundary-Layer Meteorol*. doi:[10.1007/s10546-010-9477-0](https://doi.org/10.1007/s10546-010-9477-0)

- Inagaki A, Maruyama A, Kanda M (2009) Spatial and temporal scales of coherent turbulence over outdoor reduced urban scale model. In: The 7th international conference on urban climate. Yokohama, Japan
- Inagaki A, Castillo MCL, Yamashita Y, Kanda M (2010) Numerical simulation of atmospheric turbulence within and above a cubical canopy. In: Ninth symposium on the urban environment. American Meteorological Society, Keystone
- Jeong J, Hussain F, Schoppa W, Kim J (1997) Coherent structure near the wall in a turbulent channel flow. *J Fluid Mech* 332:185–214
- Kaga A, Inoue Y, Yamaguchi K (1992) Application of a fast algorithm for pattern tracking on airflow measurement. In: Proceedings of 6th international symposium on flow visualization, pp 853–857
- Kanda M (2006) Large-eddy simulations on the effects of surface geometry of building arrays on turbulent organized structures. *Boundary-Layer Meteorol* 118:151–168
- Kanda M, Moriizumi T (2009) Momentum and heat transfer over urban-like surfaces. *Boundary-layer Meteorol* 131:385–401
- Kanda M, Moriwaki R, Kasamatsu F (2004) Large-eddy simulation of turbulent organized structures within and above explicitly resolved cube arrays. *Boundary-layer Meteorol* 112:343–368
- Kanda M, Kanega M, Kawai T, Moriwaki R (2007) Roughness lengths for momentum and heat derived from outdoor urban scale models. *J Appl Meteorol Climatol* 46:1067–1079
- Kawai T, Kanda M, Narita K, Hagishima A (2007) Validation of a numerical model for urban energy-exchange using outdoor scale-model measurements. *Int J Climatol* 27:1931–1942
- Kim J-J, Baik J-J (2004) A numerical study of the effects of ambient wind direction on flow and dispersion in urban street canyons using RNG $k-\varepsilon$ turbulence model. *Atmos Environ* 38:3039–3048
- Klein P, Clark JV (2007) Flow variability in a North American downtown street canyon. *J Appl Meteorol Climatol* 46:851–877
- Liu H, Liang B, Zhu F, Zhang B, Sang J (2003) A laboratory model for the flow in urban street canyons induced by bottom heating. *Adv Atmos Sci* 20:554–564
- Louka P, Belcher SE, Harrison RG (2000) Coupling between air flow in streets and the well-developed boundary layer aloft. *Atmos Environ* 34:2613–2621
- Louka P, Vachon G, Sini J-F, Mestayer PG, Rosant J-M (2002) Thermal effects on the airflow in a street canyon—Nantes'99 experimental results and model simulations. *Water Air Soil Pollut Focus* 2:351–364
- Macdonald RW, Griffiths RF, Hall DJ (1998) An improved method for the estimation of surface roughness of obstacle arrays. *Atmos Environ* 32:1857–1864
- Nakayoshi M, Moriwaki R, Kawai T, Kanda M (2009) Experimental study on rainfall interception over an idealized outdoor urban scale model. *Water Resour Res* 45:W04415
- Reynolds RT, Castro IP (2008) Measurements in an urban-type boundary layer. *Exp Fluids* 45:141–156
- Rotach MW (1995) Profiles of turbulence statistics in and above an urban street canyon. *Atmos Environ* 13:1473–1486
- Snyder WH, Castro IP (2002) The critical Reynolds number for rough-wall boundary layers. *J Wind Eng Ind Aerodyn* 90:41–54
- Stull RB (1988) An introduction to boundary layer meteorology. Kluwer Academic Publishers, Dordrecht, 666 pp
- Sugawara H, Ogawa H, Hagishima A, Narita K, Tanimoto J (2006) Observation of stability-influenced canyon flow patterns. In: Proceedings of 6th international conference on urban climate. Göteborg, Sweden, pp 180–183
- Takimoto H, Sato A, Michioka T, Kanda M (2009) PIV measurements on the effects of fetch lengths and atmospheric stabilities on turbulent flow over building arrays. In: Proceedings of the conference on physical modelling of flow and dispersion phenomena. Sint-Genesius-Rode, Belgium, pp F5.1–F5.9
- Uehara K, Murakami S, Oikawa S, Wakamatsu S (2000) Wind tunnel experiments on how thermal stratification affects flow in and above urban street canyons. *Atmos Environ* 34:1553–1562
- Uehara K, Wakamatsu S, Ooka R (2003) Studies on critical Reynolds number indices for wind-tunnel experiments on flow within urban areas. *Boundary-Layer Meteorol* 107:353–370
- Walton A, Cheng AYS (2002) Large-eddy simulation of pollution dispersion in an urban street canyon—Part II: Idealized canyon simulation. *Atmos Environ* 36:3615–3627
- Zhou J, Adrian RJ, Balachandar S, Kendall TM (1999) Mechanisms for generating coherent packets of hairpin vortices in channel flow. *J Fluid Mech* 287:353–396
- Zhu W, van Hout R, Luznik L, Kang HS (2006) A comparison of PIV measurements of canopy turbulence performed in the field and in a wind tunnel model. *Exp Fluids* 41:309–318